

Statistical inversion for medical x-ray tomography with few radiographs: II. Application to dental radiology

V Kolehmainen¹, S Siltanen², S Järvenpää³, J P Kaipio¹, P Koistinen³,
M Lassas³, J Pirttilä⁴ and E Somersalo⁵

¹ Department of Applied Physics, University of Kuopio, PO Box 1627, FIN-70211 Kuopio, Finland

² Instrumentarium Corp Imaging Division, PO Box 20, FIN-04301 Tuusula, Finland

³ Rolf Nevanlinna Institute, University of Helsinki, PO Box 4, FIN-00014, Finland

⁴ Invers Ltd, Tähteläntie 54 A, FIN-99600 Sodankylä, Finland

⁵ Institute of Mathematics, Helsinki University of Technology, PO Box 1100, FIN-02015, Finland

E-mail: Ville.Kolehmainen@uku.fi

Received 3 January 2003

Published 7 May 2003

Online at stacks.iop.org/PMB/48/1465

Abstract

Diagnostic and operational tasks in dental radiology often require three-dimensional information that is difficult or impossible to see in a projection image. A CT-scan provides the dentist with comprehensive three-dimensional data. However, often CT-scan is impractical and, instead, only a few projection radiographs with sparsely distributed projection directions are available. Statistical (Bayesian) inversion is well-suited approach for reconstruction from such incomplete data. In statistical inversion, *a priori* information is used to compensate for the incomplete information of the data. The inverse problem is recast in the form of statistical inference from the posterior probability distribution that is based on statistical models of the projection data and the *a priori* information of the tissue. In this paper, a statistical model for three-dimensional imaging of dentomaxillofacial structures is proposed. Optimization and MCMC algorithms are implemented for the computation of posterior statistics. Results are given with *in vitro* projection data that were taken with a commercial intraoral x-ray sensor. Examples include limited-angle tomography and full-angle tomography with sparse projection data. Reconstructions with traditional tomographic reconstruction methods are given as reference for the assessment of the estimates that are based on the statistical model.

1. Introduction

The main tool in dental radiology is the x-ray projection image that reveals inner structure of bone and teeth. However, the obvious drawback of a projection (or a panoramic) image is irreversible overlapping of structures. Certain diagnostic and operative tasks often require more precise knowledge of the three-dimensional structure of tissue than is available in single projection image. Such tasks include (Brocklebank 1997, Ekestubbe *et al* 1997, Ramesh *et al* 2002)

- Deciding whether two roots have grown together with common root canal or not.
- Detection of alveolar decrease, or bone loss between teeth.
- Implant planning.
- Finding out whether certain roots have intimate relationship with the inferior dental canal. This is related to the risk of damaging nerves when removing a tooth.
- Analysis of the form of the condylar process in the temporomandibular joint.

We consider taking a small number of projection images of the tissue from sparsely distributed directions using the dentist's regular x-ray equipment and reconstructing the 3D structure of tissue from the projections. More precisely, we consider the following two types of sparse projection data:

- (A) Sparse limited-angle data. In intraoral imaging a few projection radiographs are taken with a small digital sensor in fixed position inside the patient's mouth. Due to geometrical restrictions, the x-ray source positions are limited to a cone with opening angle significantly less than 180° .
- (B) Sparse full-angle data. In extraoral imaging the region of interest is imaged through the head from a small number of sparsely distributed projection directions.

For both data types, the projection images are often truncated due to small detector size or in order to minimize dose to vital organs. In these cases the image reconstruction has the additional complication of local tomography problem. Both data types, (A) and (B), lead to ill-posed image reconstruction problems (i.e., the solution is sensitive to measurement errors and/or the problem does not have unique solution).

It is well known that traditional CT algorithms, such as filtered backprojection, are not well-suited for projection data of type (A) or (B) since these data types violate the assumptions of those algorithms. Despite this conflict between the data and the assumptions, traditional methods have been widely used for both data types. For data type (A) a traditional reconstruction method is tuned aperture computed tomography (TACT) method (Webber 1998, Grant 1972, Ziedses des Plantes 1932), which is basically equivalent to unfiltered backprojection. For data type (B) a popular traditional method is filtered backprojection (FBP) in the case of global tomography (i.e., projections are not truncated). For the local tomography data of type (B), a usual method is Λ -tomography which has been developed for local tomography problems with non-sparse full-angle projection data (Smith and Keinert 1985, Kuchment *et al* 1995, Faridani *et al* 1992, 1997).

Statistical inversion (SI) is a well-suited approach for 3D reconstruction with both data types (A) and (B). In statistical inversion, *a priori* knowledge of the tissue is used in the image reconstruction problem in order to compensate for the incomplete information in the sparse projection data. Separate statistical models (probability distributions) are formulated for (a) the acquisition of the projection data and (b) the *a priori* information. Based on these models and the Bayes formula, a complete solution of the inverse problem is obtained as the posterior probability distribution. Final images of the target are then obtained as point estimates from the posterior distribution. In contrast to traditional reconstruction methods, the statistical approach gives natural means for the computation of confidence limits for the estimates.

We propose a statistical model for three-dimensional dental imaging. In the proposed model, we approximate the three-dimensional problem by a stack of two-dimensional problems. In the Bayesian model for each two-dimensional problem we use the following prior models:

- (i) For each 2D slice we use a total variation (TV) prior model. Total variation is a feasible prior model for dental structures since they are expected to consist of a few approximately homogeneous regions with sharp, well-defined boundaries.
- (ii) To take the 3D nature of the problem into account, a L^1 -prior is used in the model for the distance of the current slice from the previous one. This is based on the assumption that the cross-section of dental structures does not change much between two consecutive slices.
- (iii) Positivity prior, which in short means that x-rays can only attenuate and not intensify inside tissue.

To illustrate the performance of the model, results with *in vitro* sparse projection data are given. For data type (A) we consider two examples. The first example is a model problem with sparse projection data from a tooth phantom. For this test case, the ground truth is given by a full-angle reconstruction. The second example for (A) is reconstruction using truncated intraoral measurements from a realistic head phantom. For both cases, the maximum *a posteriori* (MAP) estimates are presented as reconstructions of the target. For both cases traditional tomosynthetic (backprojected) reconstructions are shown as reference images for the assessment of the statistical model. For the first test case, we will also give an illustrative example of more complete statistical inference from the posterior distribution using Markov chain Monte Carlo (MCMC) methods.

For data type (B) we consider also two examples. The first example is a model problem using full-angle sparse projection data from the tooth phantom. MAP estimates are represented as images of the target and reconstructions with the widely used filtered backprojection (FBP) method are shown as reference images. The second test case for (B) is full-angle reconstruction from sparse projection data with truncated projections from a jaw phantom. MAP estimates are represented as images of the target. Backprojection and Λ -tomography reconstructions are shown as reference images.

Application of Bayesian inversion to dental radiology appears to be new. Statistical methods have been used for data type (B) in Sukovic *et al* (2001), however, only likelihood distribution is used for the reconstruction. With the model introduced in this paper it is possible to further improve (Sukovic *et al* 2001) with simultaneous reduction in radiation dose.

This paper is organized as follows. In section 2 we discuss the transformation of digital radiographs to tomographic data. We also discuss the experimental imaging geometries used in the examples. In section 3.1 we discuss the statistical model that is used in this paper. The discussion is mainly based on the theory and models that were presented in part I of this paper. We also discuss the computation of the point estimates. A gradient-based optimization approach is given for the computation of the MAP estimate, and then computation of other usual statistics that necessitate integration is discussed. Results with the experimental data are given in section 4 and in section 5 we give conclusions.

2. From digital radiographs to tomographic data

The projection radiographs of the targets were acquired using a commercial intraoral x-ray detector Sigma and a dental x-ray source Focus⁶. As explained in section 3.2, part I of this

⁶ Sigma and Focus are registered trademarks of Instrumentarium Corp. Imaging Division.

paper, the input data of tomographic algorithms is a collection of line integrals of the unknown attenuation coefficient function. For each pixel value in each projection image we need to (a) determine the path of the detected x-ray through the pixel/voxel grid and (b) the amount of attenuation of the x-ray through that path. We discuss the transformation of the projection data in section 2.1 and the measurement geometries for the experiments in sections 2.2–2.4.

2.1. From detected pixel values to attenuation measurements

The Sigma detector is based on charge coupled device (CCD) technology and it is capable of sensing roughly 2000 grey levels. Size of the active imaging area is 34×26 mm and the resolution is 872×664 pixels. After exposure, each pixel contains a positive integer which is directly proportional to the number of x-ray quanta that hit the pixel's area.

A detected pixel value p is transformed to tomographic attenuation measurement P as follows. Let M be the logarithm of the maximum pixel value over all detector pixels. We define the tomographic data as

$$P = M - \log(p). \quad (1)$$

What kind of error is introduced by this transformation? The ideal tomographic data should be the integral of the attenuation coefficient $x(s)$ along the x-ray path L :

$$P' = \int_L x(s) ds = \log(I_0) - \log(I_1).$$

The pixel value p is directly proportional to the final intensity: $p = aI_1$. If the detector is partly illuminated by direct radiation, we have $M \approx \log(aI_0) = \log(a) + \log(I_0)$. Then

$$P = M - \log(p) \approx \log(a) + \log(I_0) - \log(a) - \log(I_1) = P'.$$

Thus, the above transformation is a feasible choice for problems in which the distance and angle of the x-ray source are fixed with respect to the detector and every projection contains some 'air-only' observations. Without such observations, $\log(I_0)$ needs to be calibrated from imaging parameters.

2.2. Experimental setup for the tooth phantom model problem

In order to get full-angle reconstructions as a reference for the limited-angle reconstructions in the model problem with the tooth phantom, we used the conventional cone beam CT-geometry, which is shown schematically in figure 1, for our laboratory experiments.

The experiments were carried out as follows. The Sigma CCD-detector and the Focus x-ray source were attached into fixed positions such that the source direction is normal to the detector array. The distance from the focal spot to the detector array was 840 mm. The tooth phantom, which was a third mandibular molar removed from a female patient of age 25, was placed on a rotating platform, so that projections from different angles can be obtained. The distance from the centre of rotation to the detector was 56 mm. Left image in figure 2 shows one raw 872×664 projection image from the experiments, the middle image shows one row (i.e., raw data for one two-dimensional slice) from the projection image and the right image shows the same row in the form of tomographic data. We note that the white triangles in the lower corners of the projection image in figure 2 do not correspond to detected radiation. They result from the rounded corners of the intraoral detector.

The purpose of the wires that are seen in the lower part of the left image in figure 2 is to give information about the location and alignment of the rotation axis in the projection images.

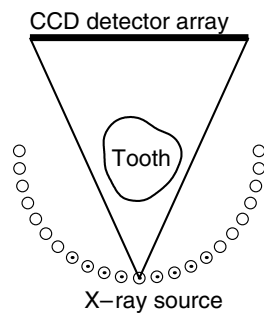


Figure 1. Cone beam imaging geometry for full-angle tomography. This geometry was used in the experiments with the tooth phantom. Circles denote the source locations for the full-angle data (23 projections from total view-angle of 187°). The projections that were used in limited-angle computations (nine projections from view-angle of 68°) are denoted by black dots within the circles. For clarity, the location and alignment of the detector with respect to the source is depicted only for one source location.

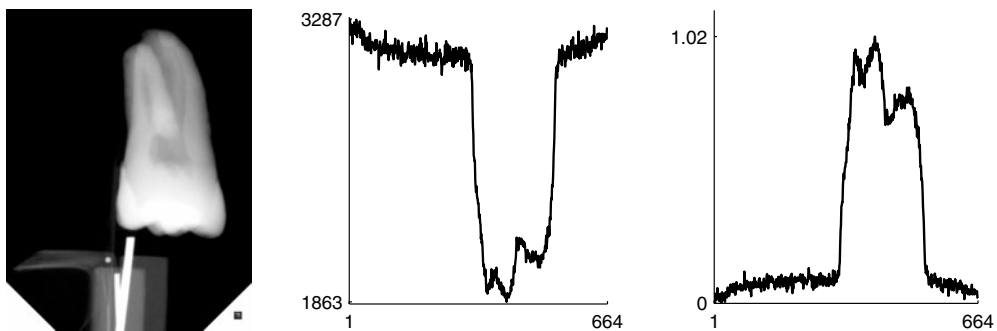


Figure 2. Left: 872×664 projection radiograph from the tooth phantom. Note that the image is shown with inverted colourmap (i.e., black corresponds to high photon counts). Middle: pixel values of the 200th row from the raw projection radiograph. Right: same row in the form of tomographic attenuation data.

In the sum image of all projections, the wires appear as a sandglass shaped object. The node of this sandglass gives rotation axis for one slice and the inclination angle of the rotation axis can be obtained by computing the normal direction to the path in sum image that is drawn by the upper end of the longer wire. The projection angles were read from a millimeter scale paper that was attached around the rotating platform of the tooth phantom.

We note that this experimental geometry corresponds to the case in which the source and detector array move on a horizontal circle. Thus, the projection directions are restricted onto a circular arc. Also, the source-to-detector distance is relatively long with respect to the physical size of the Sigma detector. These allow us to approximate the 3D reconstruction problem by a stack of two-dimensional problems with a reasonably good accuracy. The development of purely 3D methods is left to future studies.

Finally, the transpose of each of the transformed projection images corresponds to one block of the tomographic data for the 3D experiment. As an example, the left image in figure 3 shows one column (i.e., line integral data from all projections for one two-dimensional slice) of this block matrix for the data from the tooth in traditional sinogram form. The data were

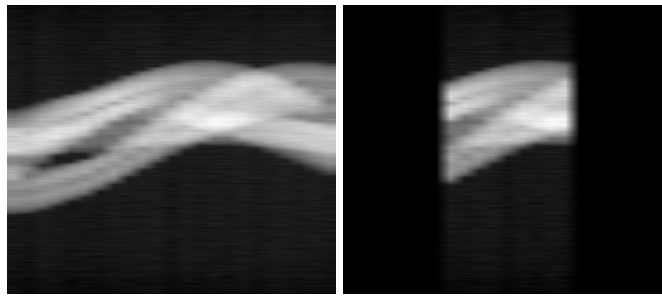


Figure 3. Sinogram for the 200th slice of the projection data from the tooth phantom. Left: projections used in this sinogram were collected from 187° angle of view (23 projections with 8.5° projection interval). Right: the 68° part of the sinogram that was used for the limited-angle reconstructions.

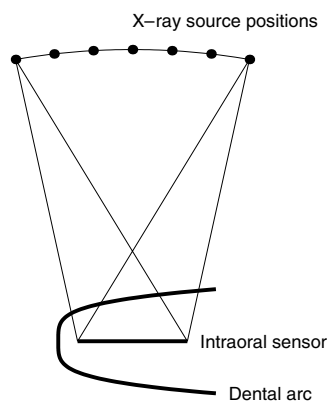


Figure 4. Imaging geometry for intraoral measurements. The detector is in fixed position inside the patient's mouth. This geometry was used in the test case with the head phantom.

collected by taking 23 projections with total 187° angle of view. Referring forward to the first model problem, which is the limited-angle reconstruction from sparse projection data, the right image in figure 3 shows the part of sinogram (nine projections with 68° angle of view) that was used in the limited-angle reconstructions.

2.3. Measurement geometry for intraoral imaging

In intraoral dental x-ray imaging, the measurement geometry is such that the detector is in fixed position inside the patient's mouth and the dentist can move the x-ray source, which is mounted on a foldable arm, with respect to the intraoral detector. This geometry is illustrated schematically in figure 4.

In this study, this geometry was used for the limited-angle experiments with the realistic head phantom. In the experiments, the Sigma detector was placed in a fixed position inside the mouth of the head phantom such that it was right behind the teeth to be imaged. The x-ray source was mounted on a foldable arm which was used to move the source on an approximately circular arc with distance of ~ 590 mm from the detector.

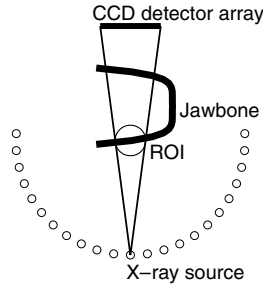


Figure 5. Cone beam imaging geometry for local tomography. This geometry was used in the last test case with the jaw bone phantom. The source positions for the experiments (23 projections from view-angle of 187°) are denoted by circles. The region of interest (ROI) is denoted by thin line. For clarity, the location and alignment of the detector with respect to the source is depicted only for one source location.

2.4. Measurement geometry for extraoral imaging

In extraoral imaging, the region of interest (ROI) is imaged from different directions through the head. Typical geometry for extraoral imaging is illustrated in figure 5. The patient is kept in fixed position. The source and the detector array are mounted onto a rotating platform that can be used to move the source and detector array to different projection angles. There are some dedicated devices for such measurements (Mozzo *et al* 1998, Sukovic *et al* 2001). We note that extraoral imaging (as depicted in figure 5) leads to local tomography problem.

Our last test case is extraoral imaging with sparse projection data from a jaw bone phantom. There the experimental setup was implemented similarly to the setup explained in section 2.2: the phantom was placed on the rotating platform and the Sigma detector and x-ray source were mounted into fixed positions. With the exception of different source-to-detector distance (1292 mm) and centre of rotation-to-detector distance (88 mm), the geometrical details of the experimental setup were the same as in section 2.2.

3. Statistical inversion in 3D dental imaging

3.1. Statistical model for dental imaging

In this section we discuss the application of the statistical inversion approach to three-dimensional dental imaging. As was discussed previously, we approximate the 3D problem by a stack of $j = 1, 2, \dots, N_{\text{sli}}$ two-dimensional problems.

Let

$$x^{(j)} = \sum_{i=1}^M x_i^{(j)} \chi_i \quad (2)$$

where χ_i is the characteristic function of pixel Ω_i in the two-dimensional pixel lattice, denote the discrete representation of the j th slice in the stack of two-dimensional slices. In the following, we will identify the function (2) by the coefficient vector $x^{(j)} = (x_1^{(j)}, x_2^{(j)}, \dots, x_M^{(j)})^T \in \mathbb{R}^M$. Further, let

$$m^{(j)} = Ax^{(j)} + \epsilon^{(j)} \quad (3)$$

denote the observation model for the j th 2D problem. In equation (3), $m^{(j)} = (m_1^{(j)}, m_2^{(j)}, \dots, m_N^{(j)})^T \in \mathbb{R}^N$ is the vector of tomographic data for j th two-dimensional slice

and $\epsilon^{(j)} \in \mathbb{R}^N$ denotes the observation noise. It should be noted that with our experimental setup, the model matrix is not the same for each 2D slice due to the possible displacement of the rotation axis between different slices $m^{(j)}$ of the projection data. Also, the size of the data vector $m^{(j)}$ may vary due to the rounded corners of the Sigma detector (see figure 2). However, due to notational simplicity, we use the notation $A \doteq A^{(j)}$ for the model matrix and $N \doteq N_j$ for the dimension of the projection data vector in the following.

The statistical model we use for dental imaging was introduced in sections 3.1, 3.2, part I of this paper. As the prior model for the two-dimensional slices $x^{(j)}$ of the dental structures we use the total variation (TV) prior. Within the discretization (2) of the 2D attenuation coefficient function, the total variation can be written as

$$\text{TV}(x^{(j)}) = \sum_{k=1}^{N_e} l_k |\Delta_k^T x^{(j)}| \tag{4}$$

where l_k is the length of the edge between the adjacent pixels $\Omega_{i_1^k}$ and $\Omega_{i_2^k}$, $\Delta_k \in \mathbb{R}^M$ is the vector

$$\Delta_k = (0, \dots, \overset{(i_1^k)}{1}, 0, \dots, 0, \overset{(i_2^k)}{-1}, 0, \dots, 0)^T$$

and N_e is the number of edges (s.t. $l_k = |\partial\Omega_{i_1^k} \cap \partial\Omega_{i_2^k}| > 0$) connecting two adjacent pixels in the 2D lattice.

The *total variation* prior density for the 2D attenuation coefficient $x^{(j)}$ is defined as

$$p_{\text{TV}}(x^{(j)}) \propto e^{-\alpha \text{TV}(x^{(j)})} \tag{5}$$

where the total variation is calculated using equation (4). The total variation prior can be considered as a feasible model for dental structures, since it has high probability density for level set type images which consist of a few (almost) constant attenuation levels which are bounded by short, well-defined boundary lines. The use of TV prior for the regularization of inverse problems has been discussed for example in Vassilevski and Wade (1997), Kaipio *et al* (2000), Persson *et al* (2001) and the use of TV constraints for image enhancement in Dobson and Santosa (1994, 1996), Dobson and Vogel (1997).

To take the three-dimensional structure of the target into account in the stack of two-dimensional reconstructions, we use a (conditional) L^1 -prior between the slices $x^{(j)}$ and $x^{(j-1)}$. Let $\hat{x}^{(j-1)}$ denote an estimate for the slice $x^{(j-1)}$ (with initialization $\hat{x}^{(0)} = 0$). Within the discrete framework, this coupling prior density can be written in the form

$$\begin{aligned} p_{L^1}(x^{(j)}|\hat{x}^{(j-1)}) &\propto \exp(-\gamma \|x^{(j)} - \hat{x}^{(j-1)}\|_{L^1}) \\ &= \exp\left(-\gamma \sum_{k=1}^M |\Omega_k| |x_k^{(j)} - \hat{x}_k^{(j-1)}|\right). \end{aligned} \tag{6}$$

The L^1 -prior is concentrated around images $x^{(j)}$ which are close to $\hat{x}^{(j-1)}$ but may have a few large deviations with small support. For an extensive discussion on this feature, see the article (Donoho *et al* 1992). We chose the model (6) based on the assumption that the cross-section of dental structures does not change much between two consecutive slices.

Taking into account the positivity prior $p_+(x^{(j)})$ for the attenuation coefficient, equation (19) in part I of this paper, and using equations (5) and (6), the overall (conditional) prior density for slice $x^{(j)}$ assumes the form

$$p(x^{(j)}|\hat{x}^{(j-1)}) \propto p_+(x^{(j)}) \exp(-\alpha \text{TV}(x^{(j)}) - \gamma \|x^{(j)} - \hat{x}^{(j-1)}\|_{L^1}). \tag{7}$$

For the observation errors $\epsilon^{(j)}$ we make the assumption that they are Gaussian with zero-mean ($\epsilon^{(j)} \sim \mathcal{N}(0, \Gamma_{\text{noise}})$) and are independent of the attenuation parameters $x^{(j)}$. Using the

theory and the likelihood model that were given in sections 3.1, 3.2, part I of this paper, the posterior density for the j th two-dimensional problem assumes the form

$$p(x^{(j)}|m^{(j)}, \hat{x}^{(j-1)}) \propto p_+(x^{(j)}) \exp(-F(x^{(j)}, \hat{x}^{(j-1)})) \quad (8)$$

where

$$F(x^{(j)}, \hat{x}^{(j-1)}) = \frac{1}{2} \|m^{(j)} - Ax^{(j)}\|_{\Gamma_{\text{noise}}^{-1}}^2 + \alpha \text{TV}(x^{(j)}) + \gamma \|x^{(j)} - \hat{x}^{(j-1)}\|_{L^1}. \quad (9)$$

As was explained in section 3.1, part I of this paper, the posterior density constitutes the complete solution of the inverse problem in the statistical sense. To summarize and visualize the statistical solution of the inverse problem one needs to compute different statistics from the posterior distribution. Most common choices include the maximum *a posteriori* (MAP) and conditional mean (CM) estimates, covariance/correlation matrices and marginal densities together with confidence intervals (Gamerman 1997, Gilks *et al* 1996, Kaipio *et al* 2000). In the following, we explain the computation of the MAP estimate and then the computation of other, integration based posterior statistics using MCMC methods is briefly discussed.

3.2. Computation of the MAP estimate

The most usual estimate from the posterior is the maximum *a posteriori* (MAP) estimate which is defined through the relation

$$p(x_{\text{MAP}}^{(j)}|m^{(j)}, \hat{x}^{(j-1)}) = \max(p(x^{(j)}|m^{(j)}, \hat{x}^{(j-1)})).$$

As discussed in section 3.5, part I of this paper, the computation of the MAP estimate from the posterior density in equation (8) amounts to finding the parameter vector that satisfies

$$x_{\text{MAP}}^{(j)} = \arg \min_{x^{(j)} \geq 0} F(x^{(j)}, \hat{x}^{(j-1)})$$

where $F(x^{(j)}, \hat{x}^{(j-1)})$ is as in equation (9). We intend to find the estimate $x_{\text{MAP}}^{(j)}$ by applying gradient based optimization methods. However, here we face two difficulties. First, the total variation and L^1 -prior functionals are non-differentiable, due to the presence of the absolute value function. To overcome this problem, we use the smooth approximation

$$|t| \approx h_\beta(t) = \frac{1}{\beta} \log(\cosh(\beta t)) \quad (10)$$

where $\beta > 0$ is a parameter adjusting the accuracy of the approximation. The approximation $h_\beta(t)$ with the value $\beta = 200$ (that is used in this study) and the absolute value function $|t|$ are shown between the interval $t \in [-0.10, 1]$ in figure 6.

Using the approximation (10), the approximate total variation is obtained as

$$\text{TV}_\beta(x^{(j)}) = \sum_{k=1}^{N_e} l_k h_\beta(\Delta_k^T x^{(j)}) \quad (11)$$

and the approximate L^1 -norm, which we denote by $L_\beta^1(\cdot)$, is obtained as

$$L_\beta^1(x^{(j)} - \hat{x}^{(j-1)}) = \sum_{k=1}^M |\Omega_k| h_\beta(x_k^{(j)} - \hat{x}_k^{(j-1)}). \quad (12)$$

Using these approximations for TV and L^1 -functionals, the objective functional (9) is approximated by a differentiable functional of the form

$$F_\beta(x^{(j)}, \hat{x}^{(j-1)}) = \frac{1}{2} \|m^{(j)} - Ax^{(j)}\|_{\Gamma_{\text{noise}}^{-1}}^2 + \alpha \text{TV}_\beta(x^{(j)}) + \gamma L_\beta^1(x^{(j)} - \hat{x}^{(j-1)}). \quad (13)$$

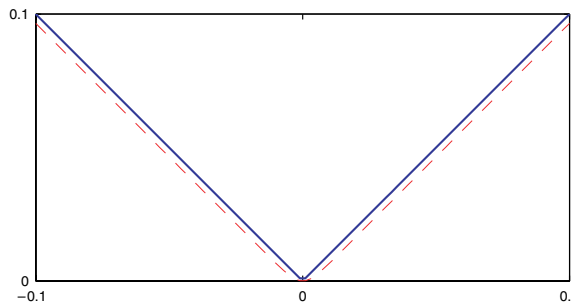


Figure 6. Absolute value function $|t|$ (solid line) and the approximation $h_\beta(t)$ (dashed line), equation (10), of the absolute value function in the interval $t \in [-0.1, 0.1]$. In the approximation $h_\beta(t)$, value $\beta = 200$ was used.

Referring to the results about singularities that are reconstructable from limited-angle data (Quinto 1993) (see also the review in section 2, part I of this paper), we show in appendix B that the MAP estimate with the TV_β -prior does not destroy any of these singularities. In other words, one can expect to see in the MAP estimate with the TV_β -prior at least the same singularities that are seen in backprojection reconstruction.

The second problem in the computation of the MAP estimate comes from the positivity constraint which is due to the positivity prior $p_+(x^{(j)})$. To take the positivity prior into account, we use an exterior point search (Fiacco and McCormick 1990). In the exterior point search, the original constrained problem is approximated by a sequence of unconstrained problems

$$x_{\text{MAP}}^{(j,t)} = \arg \min \{ F_\beta(x^{(j)}, \hat{x}^{(j-1)}) + \Upsilon^{(t)}(x^{(j)}) \} \tag{14}$$

where $\Upsilon^{(t)}(x^{(j)})$ is a penalty functional that is used to penalize the negative components of the solution $x^{(j)}$ and the superindex $x^{(j,t)}$ refers to the t th problem in the sequence of $\{t = 1, \dots, P\}$ unconstrained problems. Using a suitably chosen sequence of penalty functionals $\{\Upsilon^{(t)}(x^{(j)}), t = 1, \dots, P\}$, the exterior point method forces the sequence of solutions $\{x_{\text{MAP}}^{(j,t)}, t = 1, \dots, P\}$ (asymptotically) to the feasible region $x^{(j)} \geq 0$. Then, the solution of the constrained problem is approximated by $x_{\text{MAP}}^{(j)} \approx x_{\text{MAP}}^{(j,P)}$.

In this paper we use a penalty functional $\Upsilon^{(t)}$ of the form

$$\Upsilon^{(t)}(x^{(j)}) = \sum_{k=1}^M \phi^{(t)}(x_k^{(j)}) \tag{15}$$

where

$$\phi^{(t)}(x_k^{(j)}) = \begin{cases} \varsigma_t (x_k^{(j)})^2 & x_k^{(j)} < 0 \\ 0 & x_k^{(j)} \geq 0 \end{cases} \tag{16}$$

and $\{\varsigma_t, t = 1, 2, \dots, P\}$ is a sequence of increasing positive numbers.

In this study the MAP estimates (14) are computed using the gradient-based Barzilai–Borwein method (Barzilai and Borwein 1988).

3.3. The gradient descent method of Barzilai and Borwein

We briefly describe here the gradient-based method for unconstrained large-scale optimization introduced by Barzilai and Borwein (1988). We chose this method based on the facts that (i) the inversion of Hessian matrix is excessively heavy task due to the large dimension (M) of the

problem and (ii) the computation of the gradient for the objective functional (14) is relatively cheap, enabling relatively fast computation of multiple iterations. Further, gradient based methods are advantageous also in the sense that a more accurate approximation (larger β) for absolute value function can be used. This is due to the fact that we do not need to invert matrices that contain second derivatives of $h_\beta(t)$.

In the following, we use the notation $x^{(j,t,\ell)}$ to denote the ℓ th iterate for the t th problem in the sequence of unconstrained problems for the j th slice.

For the problem (14), the Barzilai–Borwein iteration can be written as

$$x^{(j,t,\ell+1)} = x^{(j,t,\ell)} - a_\ell^{-1} d^{(j,t,\ell)} \quad (17)$$

where the search direction is of the form

$$d^{(j,t,\ell)} = \nabla F_\beta(x^{(j,t,\ell)}) + \nabla \Upsilon^{(t)}(x^{(j,t,\ell)}) \quad (18)$$

and the step-length parameter a_ℓ is computed as

$$a_\ell = \frac{(x^{(j,t,\ell)} - x^{(j,t,\ell-1)})^T (d^{(j,t,\ell)} - d^{(j,t,\ell-1)})}{(x^{(j,t,\ell)} - x^{(j,t,\ell-1)})^T (x^{(j,t,\ell)} - x^{(j,t,\ell-1)})}. \quad (19)$$

The vector $\nabla F_\beta(x^{(j)})$ in equation (18) is of the form

$$\nabla F_\beta(x^{(j,t,\ell)}) = -A^T \Gamma_{\text{noise}}^{-1} (m^{(j)} - Ax^{(j,t,\ell)}) + \alpha \nabla \text{TV}_\beta(x^{(j,t,\ell)}) + \gamma \nabla L_\beta^1(x^{(j,t,\ell)} - \hat{x}^{(j-1)}) \quad (20)$$

where the elements of the vector $\nabla \text{TV}_\beta \in \mathbb{R}^M$ are obtained as

$$(\nabla \text{TV}_\beta(x^{(j,t,\ell)}))_m = \sum_{k=1}^{N_e} l_k h'_\beta(\Delta_k x^{(j,t,\ell)}) \Delta_{k,m} \quad (21)$$

and the elements of the vector $\nabla L_\beta^1 \in \mathbb{R}^M$ are obtained as

$$(\nabla L_\beta^1(x^{(j,t,\ell)} - \hat{x}^{(j-1)}))_m = h'_\beta(x_m^{(j,t,\ell)} - \hat{x}_m^{(j-1)}) |\Omega_m|. \quad (22)$$

In equations (21), (22) $h'_\beta(\cdot)$ denotes the first derivative of $h_\beta(\cdot)$. The entries of the vector $\nabla \Upsilon^{(t)}(x^{(j,t,\ell)})$ are of the form

$$(\nabla \Upsilon^{(t)}(x^{(j,t,\ell)}))_m = 2\zeta_t(x_m^{(j,t,\ell)}) I(x_m^{(j,t,\ell)} < 0) \quad (23)$$

where $I(x_m^{(j,t,\ell)} < 0)$ denotes the indicator function for the event $x_m^{(j,t,\ell)} < 0$.

3.4. Markov chain Monte Carlo methods

Whereas the computation of the MAP estimate is an optimization problem, the computations of other usual posterior statistics are problems of integration over a high dimensional parameter space. As discussed in part I of this paper, these tasks necessitate the use of Monte Carlo integration techniques in the case of non-Gaussian posterior density, such as the density function given in equations (8), (9).

The basic idea in Monte Carlo integration is to generate a large, representative ensemble $\{x^{(j,\ell)}, \ell = 1, 2, \dots, S\} \subset \mathbb{R}^M$ of random ‘sample images’ from the posterior density $p(x^{(j)} | m^{(j)}, \hat{x}^{(j-1)})$ and then approximate the integral of function $f(x^{(j)})$ with respect to the posterior distribution by the sample mean, that is,

$$\int_{\mathbb{R}^M} f(x^{(j)}) p(x^{(j)} | m^{(j)}, \hat{x}^{(j-1)}) dx^{(j)} \approx \frac{1}{S} \sum_{\ell=1}^S f(x^{(j,\ell)}). \quad (24)$$

Often the posterior models for inverse problems, such as the model given by equations (8), (9), are such that direct drawing of independent sample images is impossible. In Markov chain Monte Carlo (MCMC) methods the representative ensemble of (dependent) sample images is obtained by generating a realization of a Markov chain which has its stationary distribution defined by the given posterior density (Gilks *et al* 1996, Gamerman 1997). A more detailed discussion on MCMC methods is given in section 3.6, part I of this paper.

In the case of x-ray tomography the large dimension ($M > 10^4$ for a 2D slice) of the parameter space \mathbb{R}^M makes the MCMC sampling computationally a very demanding task. However, in order to give an illustrative example of more ‘complete’ statistical inference from the posterior distribution, we carry out MCMC analysis for the posterior distribution of one two-dimensional problem (i.e., for one slice $x^{(j)}$) in the first test case, which is the limited-angle problem with data from the tooth phantom. The development of efficient MCMC schemes that can be used to carry out inference for 3D reconstruction problems is left to future studies.

4. Results

4.1. Limited-angle tomography from sparse projection data of a tooth

As the first example of data type (A), see section 1, we consider the model problem of limited-angle tomography with sparse projection data (nine projections from view-angle of 68°) from a tooth phantom. As was discussed in section 2.2, the projection images from the tooth phantom were collected using the conventional CT geometry instead of using the fixed detector geometry, which is more typical geometry in clinical dental studies. However, the results for limited-angle tomography in these two geometries are qualitatively very similar. We chose to use the conventional CT geometry in order to get full-angle reconstructions as the ‘ground truth’ for the limited-angle reconstructions in this test problem. The experimental setup is explained in detail in section 2.2.

Results are shown in figures 7 and 8. The left column in figure 7 shows MAP estimates $x_{\text{MAP}}^{(j)}$ for four slices with full-angle data that were collected from view-angle of 187° with projection intervals of 8.5° (23 projections). With this set of projection images the size of the data vector $m^{(j)}$ for each two-dimensional problem is $N = 15\,272$. Figure 3 shows one slice $m^{(j)}$ of this data in a traditional sinogram form. It should be noted that if the vector $m^{(j)}$ contains values that correspond to the rounded corners of the detector, these values are neglected simply by removing respective rows from $m^{(j)}$ and A .

The domain Ω in the computation of the two-dimensional images shown in figure 7 was a $26 \times 26 \text{ mm}^2$ square which was divided into a regular $M = 166 \times 166 = 27\,556$ pixel lattice, leading to a pixel size of $\sim 0.16 \times 0.16 \text{ mm}^2$.

The left column of figure 8 shows four vertical slices of the (approximate) three-dimensional reconstruction with the full-angle data. The three-dimensional reconstruction was obtained as a stack of $N_{\text{sl}} = 600$ two-dimensional reconstructions. Each of the two-dimensional slices represents 0.045 mm thick slice of the three-dimensional data, leading to a vertical size of 26.1 mm for the images in figure 8. The horizontal size of the images in figure 8 is the same as in figure 7, that is, 26 mm. Note that the first and fourth slices in figure 8 are chosen approximately from the front and back surfaces of the tooth.

The MAP estimates with the full-angle data, left columns of figures 7 and 8, are based on the statistical model described in section 3.1. For the covariance matrix Γ_{noise} of the observation errors we used the trivial choice $\Gamma_{\text{noise}} = \sigma_n^2 I$, i.e., we assumed that the noise is statistically independent Gaussian noise with equal variance in each direction. The noise variance σ_n^2 was estimated from the projection data. This was achieved by taking one approximately

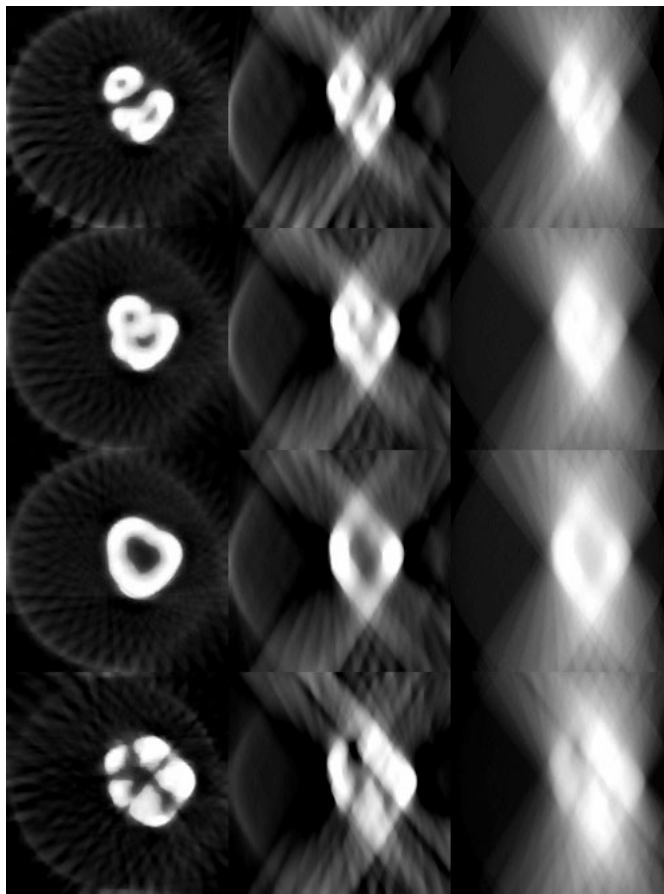


Figure 7. Left column shows MAP estimates $x_{\text{MAP}}^{(j)}$ from full-angle data with the TV_β -prior as the ‘ground truth’. The full-angle data consisted of 23 projections from total view-angle of 187° (projection interval 8.5°). The other two columns show MAP estimates with the TV_β -prior (centre column) and tomosynthetic reconstructions (right column) from limited-angle data. In the limited-angle case, nine projections from view-angle of 68° were used.

homogeneous ‘air-only’ sample (100×50 detector pixels) from one transformed projection image, and then computing estimate for σ_n^2 based on this sample. As a result, we had value $\sigma_n^2 = 0.0004$. In practice, a better estimate for the noise statistics can be obtained from a repeated set of phantom measurements and/or careful analysis of the measurement system. The determination of the accurate noise statistics for the Sigma sensor and the assessment to which extent the reconstruction results improve using a better noise model, are left to future study. The analysis given in section 3.2, part I of this paper suggests, however, that the Gaussian approximation is acceptable.

The prior parameters were chosen by visual inspection from a set of reconstructions with different parameters. With the full-angle data we used $\alpha = 1250$, $\gamma = 1250$ and $\{\zeta_t, t = 1, 2, \dots, 5\}$ was a linearly increasing sequence from 12500 to 3.75×10^5 . The parameter β in the approximation (10) for the absolute value function was $\beta = 200$. The MAP estimates were computed using the Barzilai–Borwein method. We computed six iteration

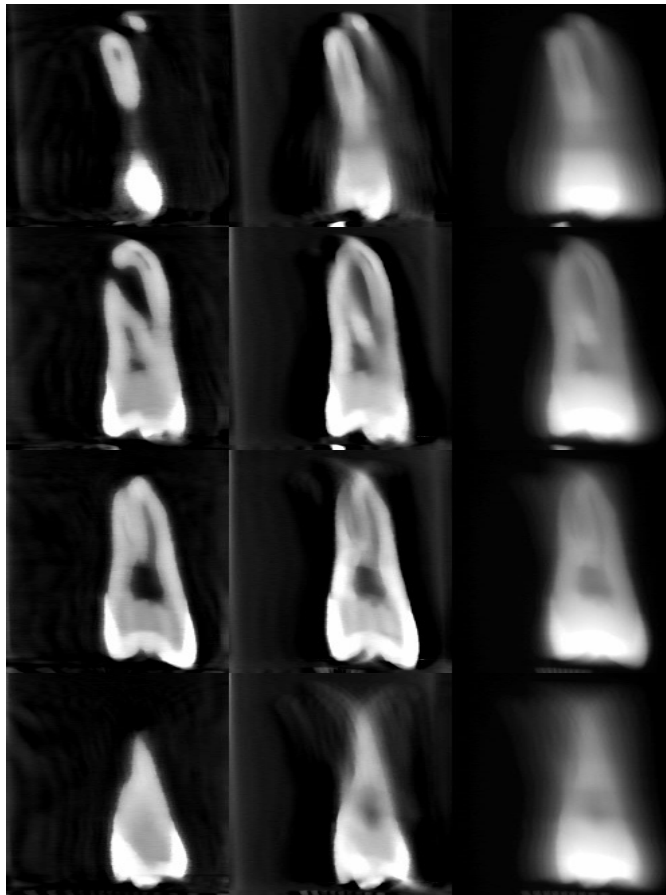


Figure 8. Left column shows vertical slices of the (approximate) 3D reconstruction from full-angle data (23 projections from view-angle of 187°) with the TV_β -prior as the 'ground truth'. The other two columns show 3D reconstruction with the TV_β -prior (centre column) and tomosynthetic reconstruction (right column) from limited-angle data. In the limited-angle case, nine projections from view-angle of 68° were used.

steps for each problem in the sequence of five unconstrained problems and then the result from the fifth unconstrained problem was used as an approximation for the MAP estimate $x_{MAP}^{(j)}$.

The second columns in figures 7 and 8 show respective slices of an approximate 3D reconstruction with limited-angle data that were collected from view-angle of 68° with projection intervals of 8.5° (nine projections). The size of the data vector $m^{(j)}$ for each slice was $N = 5976$. The right image in figure 3 shows this 68° part of the data, that was used in limited-angle computations, for one slice in sinogram form. The prior parameters in the limited-angle case were the same as in the full-angle reconstruction. The right columns in figures 7 and 8 show the respective slices for a tomosynthetic (backprojection) reconstruction from the same limited-angle data with view-angle of 68° . For details of the tomosynthesis, see Webber (1998), Grant (1972), Ziedses des Plantes (1932).

As can be seen from figures 7 and 8, the limited-angle MAP estimates with our statistical model are good in this test problem. Further, the statistical reconstructions are sharper and clearer than the traditional tomosynthetic reconstructions. This is especially evident in the



Figure 9. Statistical inference from the posterior distribution for one slice of the tooth data. Nine projections from view-angle of 68° were used as the data. Left: MAP estimate with the (smooth) TV_β -prior. Right: CM estimate with the original TV -prior.

depth direction where the information content of the limited-angle projection data is poor. This clear difference in the images gives an illustration for the effect of well-chosen prior model in limited-angle tomography. Also, note that the tomosynthetic reconstructions give an experimental illustration for the analysis about features that are reconstructable based on limited-angle projection data in Quinto (1993). A brief review of this analysis is given in section 2, part I of this paper. Given figure 7, see also figure 3 in part I of this paper.

We note that the test case in figures 7 and 8 is unrealistic (from the clinical point of view) in the sense that the tooth phantom had no surrounding tissue whereas in practical situations this is always the case. However, the purpose of this example was to test the performance of our statistical model for limited-angle tomography with sparse projections without the added complications coming from the local tomography geometry. We consider a more realistic and complicated case in section 4.3, in which we consider reconstruction from limited-angle data that was collected from a head phantom.

4.2. Example of MCMC analysis for the tooth data

To give an illustrative example of more complete Bayesian inference, we conducted MCMC analysis for one slice $x^{(j)}$ of the limited-angle data that was used in section 4.1. Since the MCMC analysis was conducted for only one slice, the coupling prior density $p_{L_1}(x^{(j)}|\hat{x}^{(j-1)})$ was not included in the posterior model.

The MAP estimate $x_{\text{MAP}}^{(j)}$ for the chosen slice with the approximate TV_β -prior is shown in the left image in figure 9. The MAP estimate was computed using the Barzilai–Borwein method. The parameters α , σ_n^2 of the posterior density, the smoothing parameter β for the approximation of absolute value function and the exterior point search parameter sequence $\{\zeta_t\}$ were the same that were used in the previous section.

Using the (approximate) MAP estimate as the initial state in the simulation, we generated an ensemble of 15 000 sample images using the Gibbs sampler (Geman and Geman 1984). For more detailed discussion on Gibbs sampling, see section 3.6, part I of this paper. It should be noted that the Gibbs sampler algorithm samples the original posterior model without any approximations to the TV and positivity priors. Detailed description of a similar algorithm that was applied to electrical impedance tomography problem can be found in Kaipio *et al* (2000), Kolehmainen (2001).

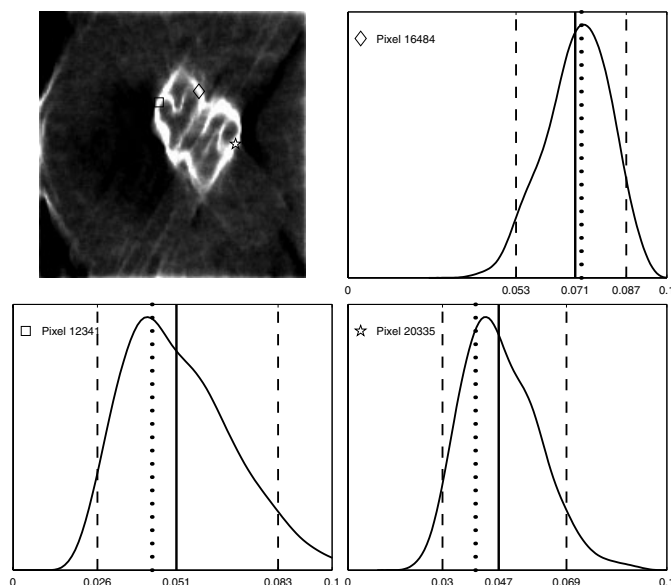


Figure 10. Statistical inference from the posterior distribution for one slice of the tooth data. Nine projections from view-angle of 68° were used as the data. Top left: estimated posterior variance for each pixel (i.e., the diagonal entries of the posterior covariance matrix). Top right and bottom: marginal densities of single pixels, which are marked in the variance image. Solid line denotes the conditional expectation, dashed lines the 90% confidence limits and the dotted line the initial value (approximate MAP value found by the Barzilai–Borwein method with TV_β -prior).

The image on the right in figure 9 shows the conditional mean estimate $x_{CM}^{(j)}$ computed as ergodic average based on the simulated Markov chain, see equation (24). The left image in the top row of figure 10 shows the estimated variances for each pixel, that is, the diagonal entries of the posterior covariance matrix. Note that the largest uncertainty in the posterior is in the directions corresponding to the pixels located at the boundaries of the tooth. The other plots in figure 10 show the marginal posterior densities of single pixels marked in the variance image.

The proper interpretation of the results in figures 9 and 10 requires care. For example, given a set of 100 realizations of the projection data from the same model, one would be tempted to say that (roughly) in 90 cases the 90% confidence limits would include the true value of the x-ray attenuation coefficient.

However, this interpretation would be incorrect. The key point here is that the posterior distribution reflects our uncertainty based on the (i) projection data and (ii) the prior information. The pitfall here is that the true attenuation coefficient may have small probability with respect to the postulated prior model. The ill-posedness of the problem with sparse tomographic data necessitates that the priors are informative with respect to certain subspaces from which the likelihood (i.e. the projection data) carries only little information. This problem is reflected in the fact that the results are usually sensitive to the selection of the prior. Summarizing, the confidence limits are reliable only in relation to our confidence in the chosen prior. Thus, the choice and careful construction of the prior model is a crucial step in statistical inversion. See also the discussion about visualization of priors in section 3.4, part I of this paper.

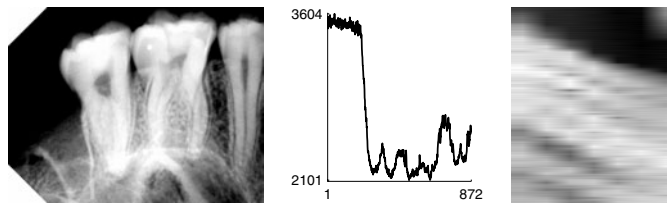


Figure 11. Left: raw 664×872 projection image from the head phantom (black corresponds to high counts). Middle: detected pixel values for the 300th row of the projection image. Right: sinogram for the 300th horizontal slice. The data consisted of seven projections that were collected from 59.7° angle of view. Note that the sinogram does not go to zero from the lower side. This reflects the fact that the problem has features of local tomography.

4.3. Limited-angle reconstruction of the head phantom

As the second test problem for limited-angle tomography for data type (A), we consider reconstruction based on sparse truncated projection data from a head phantom. Using the measurement setup that is explained in section 2.3, seven projection images were taken with approximately equal projection intervals from total view-angle of 59.7° . This represents roughly the maximum view-angle that can be used in practice. Left image in figure 11 shows one raw projection image from this dataset, the middle image shows one row of detected pixel values from the projection image and the right image shows one slice $m^{(j)}$ of the transformed data in sinogram form. The size of the vector $m^{(j)}$ is $N = 6104$. The projection images were transformed to line integral data with the approximation explained in section 2.1. With the fixed detector geometry used in this example this means that the possible angular dependency of the efficiency of the Sigma detector is neglected.

Projection angles were computed based on the images of the reference ball that was attached in front of teeth with a distance of 14 mm from the detector array. This metal ball is seen above the middle tooth in left image in figure 11. The shift of the ball in the projection images was measured, and using this information and known ball-detector distance the angles were obtained by simple trigonometric relations.

Note that in this more realistic example, all the teeth that are imaged are not visible in all projection images. This is also evident from the sinogram which is truncated from the lower side (i.e., it does not go to zero in the lower side). Thus, in addition of being a limited-angle case, the problem contains features of local tomography problem.

The results for the head phantom case are shown in figure 12. The left column shows four vertical slices of a tomosynthetic reconstruction and the right column shows respective slices of an approximate 3D reconstruction that was obtained as stack of $N_{\text{sl}} = 664$ two-dimensional MAP estimates with the TV_β -prior. In the computation of the 2D slices, the width of the two-dimensional rectangular domain $\Omega \subset \mathbb{R}^2$ was 61.25 mm and the depth was 25 mm, respectively. The domain Ω was divided into a $M = 400 \times 160 = 64\,000$ pixel grid, leading to a pixel size of $0.153 \times 0.156 \text{ mm}^2$ (width \times depth). The MAP estimates were computed using the methods described in section 3. The posterior parameters were the same as in section 4.1.

As can be seen, the statistical approach with the TV_β -prior yields good reconstructions in this more realistic and difficult test case. The effect of well-chosen prior is also seen clearly in figure 12: statistical inversion can capture relatively accurately the three-dimensional structure of the teeth despite the poor depth information content of the limited-angle projection data. Further, slices from the statistical reconstruction are sharper than tomosynthetic slices.

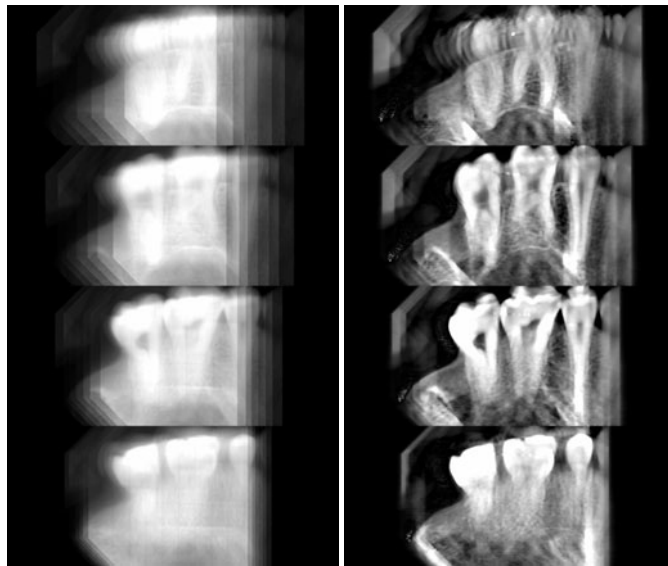


Figure 12. The left column shows four vertical slices of a tomographic, or backprojected, reconstruction from limited-angle data (seven projections from 59.7° view-angle). The right column shows respective slices of an approximate 3D reconstruction with the TV_β -prior from the same data.

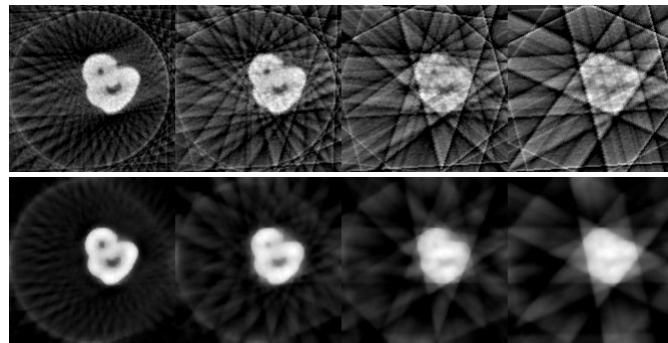


Figure 13. Full-angle (204°) reconstructions using different numbers of projections. Columns from left to right: 25 projections (projection interval 8.5°), 13 projections (17°), 7 projections (34°) and 5 projections (51°). Top row: filtered back projection. Bottom row: MAP estimates with the TV_β -prior.

4.4. Full-angle tomography with sparse projection data

As the first test problem for data type (B) we consider full-angle global tomography problem with sparse projection data. The data were collected with same imaging geometry that is explained in section 2.2 and from the same tooth phantom that was used in section 4.1.

The results for this example are shown in figure 13. Each image is a reconstruction of the same two-dimensional slice. The domain Ω and the number of pixels in the images are the same as in figure 7, that is, the domain is $26 \times 26 \text{ mm}^2$ and the number of pixels is $M = 166 \times 166 = 27\,556$ with pixel size $0.16 \times 0.16 \text{ mm}^2$. The data that were used for the reconstructions in the first column of figure 13 were collected from a view-angle of 204° with

regularly spaced projection intervals of 8.5° (total 25 projections, size of data vector $m^{(j)}$ is $N = 16\,600$). In the second column, the total view-angle was the same but only 13 regularly spaced projections were used, leading to a projection interval of 17° ($N = 8632$). In the third column number of projections was 7 with projection interval of 34° ($N = 4648$) and in the fourth column the number of projections was 5 with projection interval of 51° ($N = 3320$).

The top row shows reconstructions with the filtered back projection (FBP) algorithm and the bottom row MAP estimates with the same statistical model that was explained in section 3 and used in figures 7 and 8. The noise covariance and prior parameters for the statistical method were the same as were used in figures 7 and 8.

For the FBP reconstructions, the 664 element projection data vectors for each slice were averaged into bins of four data points, leading to data vector of 166 elements in each projection. With this operation, the pixel size for the FBP reconstruction becomes the same that was used in the statistical approach. Further, this operation improves the signal-to-noise ratio in the data for FBP, leading to less noisy reconstructions with the cost of reduced resolution. To de-emphasize the effects of (high-frequency) observation noise, Hanning-window was applied to the filtering of the projections in the frequency domain. Nearest-neighbour interpolation was used in the backprojection process. For details on theory and implementations of FBP methods, see e.g. Kak and Slaney (1988), Natterer (1986) and references therein.

As can be seen from figure 13, the statistical approach provides good reconstructions of the tooth. The MAP estimate in the second column with projection interval 17° is almost as good as the first one with projection interval of 8.5° . Whereas the MAP estimate in the third column (projection interval 34°) provides useful information about the shape and size of the tooth, the fourth one (angular projection interval 51°) gives only a crude approximation for the size and shape of the target. Also, it can be seen that the MAP estimates with the statistical model are less noisy than the reconstructions with the FBP method. It is evident from figure 13 that the statistical approach is more robust against large projection interval than the FBP method.

4.5. Local tomography from sparse projection data

As the last test case we consider a realistic example of extra-oral imaging using full-angle sparse projection data from a jaw bone phantom. This is an example of data type (B) with truncated projections. The cone beam measurement geometry for these experiments is illustrated in figure 5. Using the experimental setup explained in section 2.4, we took 23 equally spaced projection images with total view-angle of 187° (projection interval 8.5°) from the jaw bone phantom. Three of these projection images are shown in figure 14. Referring forward to the results in figure 15, the projection image on left in figure 14 was taken from the direction of positive x -axis (i.e. from right to left) with respect to the reconstructed slice. The other two projections images in figure 14 are from angles of 76.5° and 153° to counterclockwise direction with respect to the positive x -axis in the reconstructed slice, respectively.

The left image on bottom row in figure 14 shows one slice of this projection data in sinogram form. In the sinogram that is shown in the right image on the bottom row, only 12 projections with projection interval of 17° were used. As can be seen from figure 14, this test case leads to local tomography problem with full-angle sparse projection data.

The results for this example are shown in figures 15 and 16. In figure 15 each image is a reconstruction of the same two-dimensional slice. The domain $\Omega \subset \mathbb{R}^2$ in the images is $78 \times 78 \text{ mm}^2$ square which was divided into a regular $M = 498 \times 498 = 248\,004$ pixel lattice with pixel size $0.156 \times 0.156 \text{ mm}^2$. The data that were used for the reconstructions in the top row of figure 15 were collected from a view-angle of 187° with regularly spaced projection

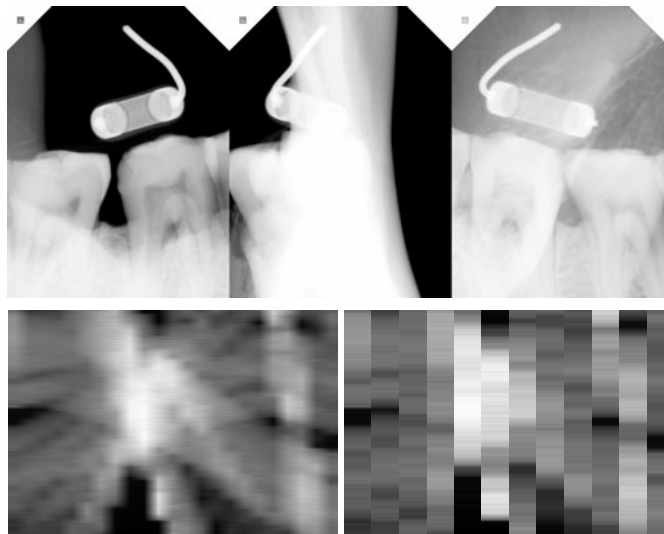


Figure 14. Top row: three 872×664 projection images from the jaw phantom. The images are (approximately) from orthogonal directions. Bottom row: sinograms for one slice of the jaw phantom data with projection intervals of 8.5° (left) and 17° (right). The projection images and the sinograms reveal clearly the local tomography nature of the reconstruction problem.

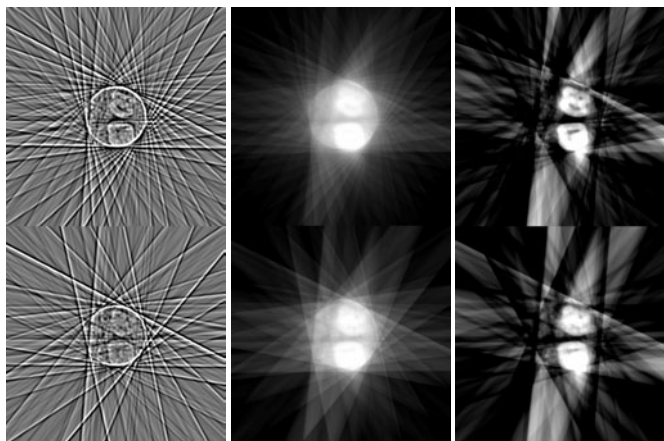


Figure 15. Reconstructions from local sparse projection data (total view-angle of 187°) from the jaw bone phantom. Top row: 23 projections with projection interval of 8.5° . Bottom row: 12 projections with projection interval of 17° . Columns from left to right: Λ -tomography, tomosynthesis (backprojection) and MAP estimates with the TV_β -prior.

intervals of 8.5° (total 23 projections, number of data $N = 15\,272$). In the bottom row, the total view-angle was the same but only 12 regularly spaced projections were used, leading to a projection interval of 17° ($N = 7968$).

The left column shows reconstruction with the Λ -tomography, middle column the tomosynthetic (backprojection) reconstructions and the right column MAP estimates with the statistical model that was explained in section 3 and used in earlier test cases.

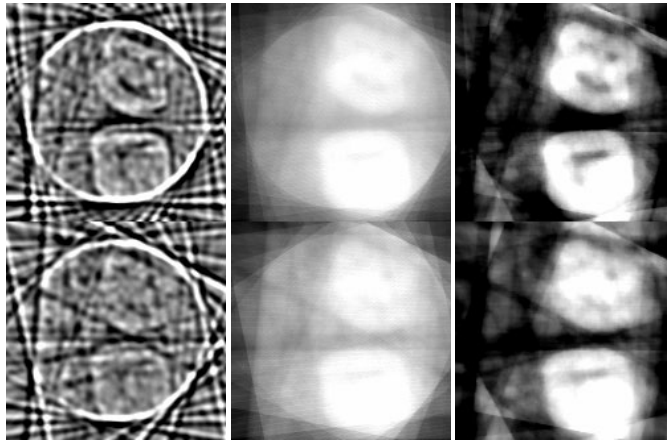


Figure 16. Regions of interest (ROI) from the local tomography reconstructions in figure 15. Rows and columns are as in figure 15.

The parameters for the statistical method were the same that were used in figures 7 and 8. The idea of Λ -tomography is discussed briefly in appendix A.

Figure 16 shows the central part (166×166 pixels) that includes the region of interest (ROI) for the respective reconstructions in figure 15.

As can be seen from figures 15 and 16, the MAP estimates with the TV_{β} -prior are relatively good also in this difficult test problem of extraoral imaging. When using all the 23 projections, the structure of the teeth that are located in the region of interest was recovered with good accuracy. In the case of using only 12 projections with projection interval of 17° , the structure of the same teeth was recovered with almost as good accuracy. A notable and typical local tomography feature in the reconstructions is the ‘back projection artefact’ type details outside the region of interest. These are evidently due to tissues that are visible possibly only in one or two projection images. Also, as can be seen from figures 15 and 16, the images that are based on the statistical approach are better than the traditional backprojection reconstructions or the Λ -tomography reconstructions. Based on figures 15 and 16, it seems that the statistical model would be useful in clinical studies of extraoral imaging.

5. Conclusions

Consider the following example of three-dimensional x-ray imaging. A dentist wants to know whether the roots of a certain tooth are close to the inferior dental canal. He takes, say, five digital intraoral projection radiographs using an x-ray source and a digital intraoral x-ray sensor choosing the directions of the images so that the images of the roots and the nerve canal are clearly separate in some of the images. The projection images together with knowledge of imaging geometry are given as input to a reconstruction algorithm. Resulting three-dimensional reconstruction is examined on computer screen and the diagnostic question answered.

The above type of three-dimensional imaging is not standard practice today. One reason for this is the lack of a flexible, fast, high-quality reconstruction algorithm for such imaging. It is evident from part I of this paper that such an algorithm should be able to use *a priori*

information of the tissue to compensate for the incomplete information provided by a few radiographs.

In this paper, we proposed a novel statistical model to three-dimensional dental x-ray imaging with sparse projection data. In the model, the three-dimensional reconstruction problem is approximated with a stack of two-dimensional problems. Our model for *a priori* information includes total variation and positivity priors for each two-dimensional slice, and the three-dimensional nature of the problem is taken into account through a coupling L^1 -prior between consecutive slices. A gradient-based optimization method was implemented for the computation of the MAP estimates and a MCMC algorithm for the computation of point estimates that necessitate integration. The performance of the model was evaluated based on *in vitro* projection data that were collected using an x-ray source and an intraoral CCD detector from a dentist's regular equipment. Reconstructions with traditional reconstruction methods were given as reference for the estimates with the statistical model. Four different test cases with sparse projection data were considered. It was seen that the statistical approach gave good results in all test cases. Furthermore, the statistical model gave improvement over traditional methods in all cases. Thus, the proposed statistical model seems promising for 3D imaging of dentomaxillofacial structures with sparse projection data.

In this study, the approximation of the three-dimensional problem by a stack of two-dimensional problems was made due to heavy computational demands of purely three-dimensional case. The computation of the approximate 3D reconstruction with the statistical method in figures 7 and 8 took approximately 6 h using MatLab (version 6) on a PC with a 1 GHz Pentium processor (number of unknowns for each 2D slice $M = 27\,556$). The computation time for the respective 3D TACT reconstruction with the same equipment was 4 min. For the reconstructions in figure 12 the respective computation times were approximately 8 h for the statistical method and 6 min for TACT (number of unknowns for each 2D slice $M = 64\,000$). Although the computation times are long with the MatLab-implementation, we believe that the computation times can be reduced to a clinically acceptable level with a sophisticated implementation on a more basic level programming platform. Preliminary tests with an optimized code give computation times less than 10 min for the reconstruction of 3D volume with clinically acceptable resolution.

The computation of the purely three-dimensional reconstructions (number of unknowns $M \gg 10^6$) with our current implementation and devices is not possible due to the excessive memory requirement of matrix A . However, the extension of the methods to purely 3D reconstruction is one of the main topics in the future work. This work is under way.

The development of more effective MCMC codes is also a topic of future work. These are more likely to be realizable in cases in which the prior model and structure of the tissue can be well described in a lower dimensional parametric basis. The approximations of different tissues by low dimensional parametric models are one topic of future work.

We also wish to start *in vivo* tests with the proposed approach in the near future. In addition to dental imaging, we believe that the proposed statistical model can also prove to be useful in other applications with 'level set' type targets.

Acknowledgments

This work was supported by the National Technology Agency of Finland (TEKES, contracts 40202/01 and 40288/02), the Saastamoinen Foundation and the Finnish Academy of Science and Letters. We also wish to thank the Finnish IT Center for Science (CSC) for providing computational resources. S Siltanen thanks Richard Webber for inspiring discussions.

Appendix A. Λ -tomography

A traditional reconstruction method that has been developed for local tomography is the so-called Λ -tomography. As in the main body of this paper, let $s \in \Omega \subset \mathbb{R}^2$ denote the position vector and $x: \Omega \mapsto [0, \infty)$ denote the x-ray attenuation coefficient function. The idea of Λ -tomography is based on the result that it is possible to recover Λx , where Λ is a Calderón operator, instead of the attenuation coefficient x itself from continuous local full-angle data (Smith and Keinert 1985, Kuchment *et al* 1995, Faridani *et al* 1992, 1997).

The Calderón operator Λ is defined using the Fourier transform as

$$\widehat{\Lambda x}(\xi) = |\xi| \hat{x}(\xi)$$

where $\hat{x}(\xi) = \int_{\mathbb{R}^2} \exp(-is\xi)x(s) ds$ for any $\xi \in \mathbb{R}^2$. This is satisfactory since Λ acts very much like a differential operator and enhances jumps (edges) of x . Further, it does not introduce sharp artefacts, only blurred ones. However, values of the attenuation coefficient x cannot be read from Λx , only the jumps are faithfully recovered.

The following reconstruction formula is due to Smith and Keinert (1985), see also Faridani *et al* (1992). We follow the notation of (Bingham (1998), formula (3.33)) and write the reconstruction formula as

$$e * (\Lambda x) = C \int_0^{2\pi} \int_0^{2\pi} \Delta P_\theta e(E_\theta(s - a))(\mathcal{D}_a x(\theta) + \mathcal{D}_a x(-\theta)) |a \cdot \vec{\theta}| d\phi d\theta \tag{A.1}$$

where $a = a(\phi) = R(\cos \phi, \sin \phi)$ is the location of the x-ray source, C is a constant, e is a smooth point spread function that approximates the Dirac delta function, Δ is the Laplace operator, P_θ is the parallel beam tomographic data (i.e., transformed projection radiograph), angle θ defines a unit vector $\vec{\theta} = (\cos(\theta), \sin(\theta))$ which in turn specifies the propagation direction of the x-rays (travelling from point a to direction $\hat{\theta}$), \mathcal{D}_a is the divergent beam (or fan-beam) tomographic data, θ is a unit vector parametrized by angle θ , E_θ is orthogonal projection onto $\vec{\theta}^\perp$ and $*$ denotes two-dimensional convolution.

The use of the point spread function e eliminates infinite values of Λf . Let $e: \mathbb{R}^2 \rightarrow \mathbb{R}$ be the radial function defined by

$$e(r) = \begin{cases} \frac{\pi}{5}(r + 1)^4(r - 1)^4 & \text{for } 0 \leq r \leq 1 \\ 0 & \text{for } 1 < r. \end{cases} \tag{A.2}$$

Note that $\int e = 1$. The function $\Delta P_\theta e$ can be computed explicitly.

In the Λ -tomography reconstruction shown in figure 15, the size of the square domain is $78 \times 78 \text{ mm}^2$ and the radius of the point spread function in (A.2) is 1 mm. The number of x-rays in each projection was 664.

Appendix B. Reconstruction of singularities with the TV_β -prior

In this appendix we consider singularities appearing in the MAP estimate with the TV_β -prior. The purpose is to show that the TV_β -prior does not destroy any of the singularities that are reconstructable based on the limited-angle data alone.

We consider the continuous model, where $x = x(s)$ is the attenuation function defined in domain $\Omega \subset \mathbb{R}^3$ and the measured data correspond to the line integrals

$$m(L) = \mathcal{A}x(L) + \epsilon(L) \quad \mathcal{A}x(L) = \int_L x(s) ds.$$

Here the variable L is a line connecting a source to detector D , where D is assumed to be a subset of a plane. The line L is assumed to hit the detector D non-tangentially. We denote

by G the open set of lines L along which we can do measurements and introduce coordinates on G by using the point $(\zeta_1, \zeta_2) \in D$ where L intersect D and two angles (α_1, α_2) related to the direction of the line L . Then \mathcal{A} defines a continuous operator $\mathcal{A}: L^2(\Omega) \rightarrow L^2(G)$ where G has a measure $\mu = d\zeta_1 d\zeta_2 d\alpha_1 d\alpha_2$. This operator has adjoint $\mathcal{A}^*: L^2(G) \rightarrow L^2(\Omega)$. The composition of these operators defines the unfiltered backprojection operator $\mathcal{A}^*\mathcal{A}$: indeed, using unfiltered backprojection algorithm with limited-angle data $m = \mathcal{A}x$ corresponds to computation of $\mathcal{A}^*\mathcal{A}x$ (Natterer 1986).

It is well known that certain singularities of x can be seen in backprojection algorithm (Quinto 1993), see also the review in section 2, part I of this paper. For instance, assume that function x has a jump across surface S . If some line $L \in G$ is tangent to the surface S at point s , then the backprojection reconstruction $\mathcal{A}^*\mathcal{A}x$ is also singular at point s (in fact, the singularity is not as strong as the original singularity).

Mathematically speaking, we say that the pair of a point s and a direction ξ is in the wave-front set of function x if the function x is singular at point s in direction ξ . This is denoted by $(s, \xi) \in WF(x)$ (for precise definition, see Hörmander (1990)). For instance, if x is a piecewise smooth function that jumps across a surface S , then the wave-front set of x consists of pairs (s, ξ) where $s \in S$ and ξ is a normal vector of S at s . The points s which do not have a neighbourhood where x is infinitely differentiable are called singular points and their set is called singular support of x and denoted by $\text{singsupp}(x)$.

Let now $H \subset \Omega$ be a set of those points s for which there is $(s, \xi) \in WF(x)$ such that ξ is orthogonal to some line $L \in G$. In other words, $H \subset \text{singsupp}(x)$ is the set of those points where some measurement line is tangent to a ‘jump’ of function x . We call H the set of the observable singularities.

It is known that the backprojection algorithm can reconstruct observable singularities,

$$H \subset \text{singsupp}(\mathcal{A}^*\mathcal{A}x)$$

see e.g. Quinto (1993). Next we show that the same property is true for MAP reconstruction with TV_β -prior. Assume that we have obtained (virtually errorless) measurements from an attenuation function $x_0 \in L^2(\Omega)$. This means that we are given $m = \mathcal{A}x_0$.

We recall that the MAP estimate is obtained from the minimization problem

$$\min_x F(x)$$

where x is compactly supported function in $\Omega \subset \mathbb{R}^3$ and

$$F(x) = \int_G (\mathcal{A}x(L) - m(L))^2 \mu(dL) + \sum_{j=1}^3 \int_\Omega h_\beta(\partial_j x(s)) ds$$

where $\partial_j x = \frac{\partial x}{\partial s_j}$ are partial derivatives of $x(s)$ and h_β is defined by equation (10). Let x be the function which minimizes $F(x)$. Then the first variation of F , which we next compute, must vanish at x . Let v be a function which vanishes in $\partial\Omega$. Then using integration by parts,

$$\begin{aligned} \lim_{t \rightarrow 0} \frac{F(x + tv) - F(x)}{t} &= \int_G 2(\mathcal{A}x - m)(L) \mathcal{A}v(L) \mu(dL) + \sum_{j=1}^3 \int_\Omega h'_\beta(\partial_j x(s)) \partial_j v(s) ds \\ &= \int_\Omega \left(2\mathcal{A}^*(\mathcal{A}x - m)(s) - \sum_{j=1}^3 \partial_j (h'_\beta(\partial_j x(s))) \right) v(s) ds \end{aligned}$$

where h'_β is the derivative of the function $h_\beta: \mathbb{R} \rightarrow \mathbb{R}$. Since x minimizes $F(x)$, the above integral has to vanish for any function v . Thus we see that minimizer x satisfies

$$2\mathcal{A}^*\mathcal{A}x(s) - \sum_{j=1}^3 \partial_j(h'_\beta(\partial_j x(s))) = 2\mathcal{A}^*m(s) = 2\mathcal{A}^*\mathcal{A}x_0(s).$$

Assume that $s \in H$. Then the right-hand side $\mathcal{A}^*\mathcal{A}x_0$ is not smooth. Thus, if the minimizer x would be smooth at s , we see that the left-hand side should be smooth which would be a contradiction. This shows that $s \in H$ implies also $s \in \text{singsupp}(x)$, that is,

$$H \subset \text{singsupp}(x).$$

In other words, at least all the discontinuities that are seen with the standard backprojection method can be seen with approximative TV priors. Note that above computation does not say anything about possible artefact singularities that may appear.

References

- Barzilai J and Borwein J M 1988 Two point step size gradient method *IMA J. Numer. Anal.* **8** 141–8
- Bingham K 1998 Mathematics of local x-ray tomography *Master's Thesis* Helsinki University of Technology (<http://www.math.hut.fi/kenny/opi/diplomityo/dtyo.html>)
- Brocklebank L 1997 *Dental Radiology—Understanding the X-Ray Image* (Oxford: Oxford University Press)
- Dobson D C and Santosa F 1994 An image enhancement technique for electrical impedance tomography *Inverse Problems* **10** 317–34
- Dobson D C and Santosa F 1996 Recovery of blocky images from noisy and blurred data *SIAM J. Appl. Math.* **56** 1181–98
- Dobson D C and Vogel C R 1997 Convergence of an iterative method for total variation denoising *SIAM J. Numer. Anal.* **34** 1779–91
- Donoho D L, Johnstone I M, Hoch J C and Stern A S 1992 Maximum entropy and the nearly black object *J. R. Statist. Ser. B* **54** 41–81
- Ekestubbe A, Gröndahl K and Gröndahl H-G 1997 The use of tomography for dental implant planning *Dentomaxillofac. Radiol.* **26** 206–13
- Faridani A, Finch D V, Ritman E L and Smith K T 1997 Local tomography II *SIAM J. Appl. Math.* **57** 1095–127
- Faridani A, Ritman E L and Smith K T 1992 Local tomography *SIAM J. Appl. Math.* **52** 459–84
- Faridani A, Ritman E L and Smith K T 1992 Examples of local tomography *SIAM J. Appl. Math.* **52** 1193–8 (a reorganization of the examples which became disorganized while the above article was in press)
- Fiacco A V and McCormick G P 1990 *Nonlinear Programming: Sequential Unconstrained Minimization Techniques* (Philadelphia: SIAM)
- Gamerman D 1997 *Markov Chain Monte Carlo—Stochastic Simulation for Bayesian Inference* (London: Chapman and Hall)
- Geman S and Geman D 1984 Stochastic relaxation, Gibbs distributions and the Bayesian restoration of images *IEEE Trans. Pattern. Anal. Mach. Intell.* **6** 721–41
- Gilks W R, Richardson S and Spiegelhalter D J 1996 *Markov Chain Monte Carlo in Practice* (London: Chapman and Hall)
- Grant D G 1972 Tomosynthesis: a three-dimensional radiographic imaging technique *IEEE Trans. Biomed. Imaging* **19** 20–8
- Hörmander L 1990 *The Analysis of Linear Partial Differential Operators: I. Springer Study Edition* (Berlin: Springer) xii+440 pp
- Kaipio J P, Kolehmainen V, Somersalo E and Vauhkonen M 2000 Statistical inversion and Monte Carlo sampling methods in electrical impedance tomography *Inverse Problems* **16** 1487–522
- Kak A C and Slaney M 1988 *Principles of Computerized Tomographic Imaging* (Piscataway, NJ: IEEE)
- Kolehmainen V 2001 Novel approaches to image reconstruction in diffusion tomography *PhD Thesis* Kuopio University Publications C. Natural and Environmental Sciences 125 (<http://venda.uku.fi/vkolehma/>)
- Kuchment P, Lancaster K and Mogilevskaya L 1995 On local tomography *Inverse Problems* **11** 571–89
- Mozzo P, Procacci C, Tacconi A, Tinazzi Martini P and Bergamo Andreis I A 1998 A new volumetric CT machine for dental imaging based on the cone-beam technique: preliminary results *Eur. Radiol.* **8** 1558–64
- Nair M K 1998 Tuned aperture computed tomography and detection of recurrent caries *Caries Res.* **32** 23–30

- Natterer F 1986 *The Mathematics of Computerised Tomography* (New York: Wiley)
- Persson M, Bone D and Elmqvist H 2001 Total variation norm for three-dimensional iterative reconstruction in limited view angle tomography *Phys. Med. Biol.* **46** 853–66
- Quinto E T 1993 Singularities of the X-ray transform and limited data tomography in \mathbb{R}^2 and \mathbb{R}^3 *SIAM J. Math. Anal.* **24** 1215–25
- Ramesh A, Ludlow J B, Webber R L, Tyndall D A and Paquette D 2002 Evaluation of tuned-aperture computed tomography in the detection of simulated periodontal defects *Oral Maxillofacial Radiol.* **93** 341–9
- Ruttimann U E, Groenhuis R A J and Webber R L 1984 Restoration of digital multiplane tomosynthesis by a constrained iteration method *IEEE Trans. Med. Imaging* **3** 141–8
- Schafer R W, Merserau R M and Richards M A 1981 Constrained iterative restoration algorithms *Proc. IEEE* **69** 432–50
- Smith K T and Keinert F 1985 Mathematical foundations of computed tomography *Appl. Opt.* **24** 3950–7
- Sukovic P, Brooks S, Perez L and Clinthorne N 2001 DentoCAT—A Novel Design of a Cone Beam CT Scanner for Dentomaxillofacial Imaging: Introduction and Preliminary Results *CARS 2001* ed H U Lemke, M W Vannier, K Inamura, A G Farman and K Doi pp 659–64
- Vassilevski P S and Wade J G 1997 A comparison of multilevel methods for total variation regularization *El. Trans. Num. Meth.* **6** 255–70
- Webber R L 1998 Method and system for creating three-dimensional images using tomosynthetic computed tomography *US Patent Application* 09/034, 922, filed on March 5, 1998
- Webber R L, Horton R A, Tyndall D A and Ludlow J B 1997 Tuned aperture computed tomography (TACT) Theory and application for three-dimensional dento-alveolar imaging *Dentomaxillofacial Radiol.* **26** 53–62
- Webber R L, Horton R A, Underhill T E, Ludlow J B and Tyndall D A 1996 Comparison of film, direct digital, and tuned aperture computed tomography images to identify the location of crestal defects around endosseous titanium implants *Oral Surg. Oral Med. Oral Pathol.* **81** 480–90
- Webber R L and Messura J K 1999 An *in vivo* comparison of diagnostic information obtained from tuned-aperture computed tomography and conventional dental radiographic imaging modalities *Oral Surg. Oral Med. Oral Pathol.* **88** 239–47
- Ziedses des Plantes 1932 Eine neue Method zur Differenzierung der Röntgenographie *Acta Radiol.* **13** 182–92